International Journal of Technology

http://ijtech.eng.ui.ac.id

Research Article

Magnetic Nanocomposite of Hydroxyapatite/Co-doped $ZnFe_2O_4$ Synthesized by Green Technology: Structure, Character, and Application

Rahmayeni [1,*], Rifky Farhan [1], Zilfa [1], Tio Putra Wendari [1], Yeni Stiadi, Zulhadjri [1]

[1]*Department of Chemistry, Faculty of Mathematics and Natural Sciences, Universitas Andalas, Kampus Limau Manis, Padang 25163, Indonesia*

[*]Corresponding author: *rahmayenni@sci.unand.ac.id;* Tel.: +62-81363100506; Fax: 075171681

Abstract: This research aimed to develop hydroxyapatite/Co-doped-$ZnFe_2O_4$ with a mole ratio of Co:Zn of 0.1:0.9 (HA/$Co_{0.1}Zn_{0.9}Fe_2O_4$) nanocomposites by hydrothermal method using waste from Pensi clam shells as a calcium source for the synthesis of hydroxyapatite. Nanocomposites were applied to remediate organic contaminants and metal ions in water. Various characterization methods confirmed the successful fabrication of HA/$Co_{0.1}Zn_{0.9}Fe_2O_4$ magnetic nanocomposite. X-ray diffraction (XRD) pattern showed distinct peaks indicating the formation of nanocomposite, and no impurities were observed. Fourier Transform Infrared (FTIR) analysis shows the absorption bands at wave numbers 482 cm^{-1} and 534 cm^{-1}, signifying the existence of M-O vibrations for the octahedral and tetrahedral sides of the ferrite contained in the nanocomposite. Nanocomposites exhibit superparamagnetic behavior, with a saturation magnetization ranging from 0.64 to 2.047 emu/g. The energy gap values in the visible light spectrum are between 2.25 and 2.4 eV. Brunauer-Emmett-Teller (BET) method was used to determine the specific surface area of nanocomposites, producing 32.01 m^2/g for those with a HA: $Co_{0.1}Zn_{0.9}Fe_2O_4$ ratio of 16:4. The composite exhibited 92.51% Cd(II) metal ions adsorption and 98.65% dye degradation. These magnetic nanocomposites have the potential to serve as an efficient and environmentally friendly sorbent for Cd(II) ions and as a catalyst for wastewater dye degradation.

Keywords: Green technology; HA/$Co_{0.1}Zn_{0.9}Fe_2O_4$; Pensi calm shells; Photocatalyst; Superparamagnetic

1. Introduction

Industrial waste is progressively a significant source of water pollution. Various industries such as printing, textiles, chemicals, electronics, pharmaceuticals, and machinery manufacturing contaminate water bodies. Chemicals, electronics, and pharmaceuticals are also contributing factors in this contamination process (Desalegn et al., 2020). These industries contribute to many contaminants, such as dyes, heavy metals, phenols, herbicides, insecticides, and medications, leaking into the aquatic environment as byproducts without adequate treatment (Elgarahy et al., 2021). The pollutants pose significant threats to human health and aquatic organisms (Tamjidi et al., 2019). According to results, many methods have been used to address the issue of water environmental pollution, including coagulation, membrane processes, activated carbon adsorption, ozonation, adsorption, microbial breakdown, and electrochemical removal, (Handayani et al., 2024;

This work was supported by the Direktorat Riset, Teknologi, dan Pengabdian kepada Masyarakat (DRTPM) funded by Penelitian Fundamental with Contract Number of 012/E5/PG.02.00.PL/2023.

https://doi.org/10.14716/ijtech.v16i5.7291
Received September 2024; Revised Januari 2025; Accepted March 2025

Madkhali et al., 2023; Karamah et al., 2019). The major limitations of each method include the difficulty in sludge formation, high chemical usage, increased operational costs, and the potential transfer of pollutants between stages. According to environmentalists and research carried out recently, there is a growing interest in wastewater pollution caused by dyes and heavy metal ions (Kartika et al., 2023), as this is a severe environmental concern in both developed and developing countries. Various synthesized materials have been utilized to reduce the environmental impacts of water pollutants. This includes the use of catalysts to degrade dyes and adsorbent materials to extract metal ions (Rahmayeni et al., 2023). Hernández used *Eichhornia crassipes* as an adsorbent to eliminate methyl orange and methylene blue from residual solutions (Hernández et al., 2022). Yue et al. synthesized a cellulose-based adsorbent designed for the removal of both anionic and cationic dyes (Yue et al., 2019). Ubando et al. have explored microalgae as a viable and sustainable biosorbent for the removal of heavy metals in wastewater treatment processes (Ubando et al., 2021).

Hydroxyapatite, with the molecular formula $Ca_{10}(PO_4)_6(OH)_2$, possesses excellent biocompatibility and bioactivity, along with a high adsorption capacity and a large surface area, making it suitable for both dye removal and metal ion adsorption. (Supriyono et al., 2023). Because it is more affordable and natural, made from natural materials like bone, limestone, and shells, hydroxyapatite is the preferable material for some purposes such as dental implants, drug delivery, cosmetics, etc. (Rimus et al., 2024; Supriyono et al., 2023). However, due to its difficulty separating from the liquid, utilizing hydroxyapatite alone is less economical. Therefore, it is necessary to modify hydroxyapatite to work more optimally, adsorb dyes in the visible light area, and can be separated from the liquid. Then, it can be reused to make the following process more efficient. Combining spinel ferrite nanoparticles (MFe_2O_4) with hydroxyapatite is a viable option (Sery et al., 2021).

Recently, ferrite spinel-based materials and their composites have been extensively studied and used as water dye degradation catalysts. Spinel ferrites featuring one metallic ion in the formula $M(II)Fe_2O_4$ such as $CoFe_2O_4$, $NiFe_2O_4$, $CuFe_2O_4$, and $ZnFe_2O_4$, exhibit remarkable magnetic properties (Ganesan et al., 2024; Rahmayeni et al., 2021). At the nanoscale, these spinel ferrites showed exceptional physical and chemical characteristics which renders them suitable for a range of applications, such as supercapacitors, semiconductors, catalysts, and cathode for olid oxide fuel cells (Fatah et al., 2023). The combination of spinel ferrite (MFe_2O_4) compounds with hydroxyapatite creates composites that have improved characteristics over their original form. Nanocomposites of spinel ferrite with hydroxyapatite have been synthesized according to various reports. A novel magnetic $Zn/HAP/MgFe_2O_4$ nanocomposite was effectively produced in three stages and used as a catalyst for the degradation of malachite green dye (Das and Dhar, 2020a). A zinc ferrite nanocomposite encapsulated in hydroxyapatite was synthesized for the removal of cadmium (II) from aqueous solutions. The results showed that the composite could eliminate 89.6% of Cd(II) ions from the solutions under optimal reaction conditions (Das and Dhar, 2020b). A novel magnetic nanocomposite, containing Sn(II)-incorporated hydroxyapatite (HAp) embedded in nickel ferrite ($NiFe_2O_4$@-HAp-Sn^{2+}), has been successfully produced using a simple method. Nanocomposite displayed exceptional photocatalytic efficiency in removing rhodamine B dye (Das et al., 2021). A bentonite/$CoFe_2O_4$/hydroxyapatite composite has been created to adsorb Pb(II) from wastewater (Desalegn et al., 2020). Zinc ferrite/hydroxyapatite ceramic with nano-sized grains was fabricated through a solid-state reaction process using chicken eggshells and was selected to be a calcium source for synthesizing HAp had been conducted. The research on the $CuFe_2O_4$@hydroxyapatite composite for the environmental remediation of certain heavy metal ions was also carried out by Sery et al. (2021) and Ibrahim et al. (2020).

$ZnFe_2O_4$ is one of the spinel ferrite materials that can be mixed with hydroxyapatite. These nanoparticles are stable spinel ferrite materials with low magnetic properties. To improve magnetic properties, doping spinel ferrite with metal ions such as cobalt and others can be applied. According to Padhan et al. (2019), doping spinel ferrite with metal elements can improve magnetic characteristics, enabling it to be more strongly attracted to external magnetic fields (Padhan et al.,

2023). Gómez et al. synthesized Co^{2+} doped $ZnFe_2O_4$ with ratios ranging from x = 0.0 to 1.0 using the co-precipitation method. The introduction of Co^{2+} doping at a ratio of x = 0.1 enhanced the magnetic properties of $ZnFe_2O_4$, transitioning it from paramagnetic to superparamagnetic (Gómez et al., 2018). In this research, a green synthesis method was introduced to create nanocomposite consisting of hydroxyapatite and Co-doped $ZnFe_2O_4$ with a mole ratio of Co:Zn of 0.1:0.9 ($HA/Co_{0.1}Zn_{0.9}Fe_2O_4$). The food waste of Pensi clam shells (*Corbicula moltkiana*) is utilized as a calcium carbonate source for hydroxyapatite synthesis. These Pensi clam shells were collected from Lake Singkarak in West Sumatra. Their high calcium content makes them a viable calcium oxide (CaO) source for producing hydroxyapatite (Panda et al., 2021). Nanocomposites were synthesized using the hydrothermal method due to the simplicity of synthesis with gambir leaf extract as the medium. This extract, abundant in secondary metabolite compounds, acts as a capping agent (Labanni et al., 2019). These compounds prevent particle agglomeration by regulating particle growth and reducing particles' surface energy (Rahmayeni et al., 2022; Javed et al., 2020). It is expected that the resulting nanocomposites could function as an adsorbent and photocatalyst. The ability of $HA/Co_{0.1}Zn_{0.9}Fe_2O_4$ nanocomposites to adsorb Cd(II) metal ions in water was determined. Heavy metal ion Cd(II) in water is often produced from automotive and battery waste (Lei et al., 2019). The photocatalytic performance of the synthesized nanocomposites was analyzed by evaluating their capacity to degrade direct red 81 dye. Direct red 81 ($C_{29}H_{19}N_5Na_2O_8S_2$), commonly found in textile industry wastewater, is notoriously difficult to decompose naturally (Hassaan et al., 2022; Dehghani et al., 2018). In this research, various parameters related to photocatalytic and adsorption processes were investigated. This involved determining the optimal catalyst amount, contact time, and concentrations of dyes or metal ions to evaluate the remediation efficiency of the synthesized nanocomposite in removing dyes and metal ions from wastewater.

2. Methods

2.1. Materials

In this research, the materials used were purchased from Merck and included $CdCl_2.H_2O$, $(NH_4)_2HPO_4$, HNO_3, $Zn(NO_3)_2.4H_2O$, $Co(NO_3)_2.6H_2O$, $Fe(NO_3)_3.9H_2O$ and NaOH. Additionally, deionized water and NH_4OH were used, and Direct Red 81 ($C_{29}H_{19}N_5Na_2O_8S_2$) served as the model dye for the experiments obtained from a textile factory in West Sumatra. Pensi (*Corbicula molkiana*) clam shells were collected from Lake Singkarak in West Sumatra, Indonesia, while gambir leaf was sourced from the agricultural fields of the Faculty of Agriculture at Andalas University.

2.2. Extraction process of gambir leaf

Leaf of Gambir (*Uncaria gambir* Roxb.) was collected from the experimental garden located at the Faculty of Agriculture, Andalas University. The fresh leaf was carefully washed several times to eliminate dust and impurities. The leaf was then shade-dried at room temperature for about 5 days. Once fully dried, the leaf was ground into a fine powder using a grinder and stored in a sterile container. For the extract preparation, 10 grams of gambir leaf powder were combined with 100 mL of distilled water and stirred at 60°C for 2 hours. After stirring, the solution was filtered, and the resulting filtrate was kept in a refrigerator until it was needed for the synthesis of nanocomposites (Labanni et al., 2019).

2.3. Synthesis of hydroxyapatite (HA) from Pensi clam shells

Pensi (*Corbicula moltkiana*) clam shells were collected from Singkarak Lake in West Sumatera and processed according to methods established by previous research. Initially, shells were washed with water and dried at 110°C. Shells were then ground into a fine powder using a Fritsch Pulverisette 16 grinder, and the powder was calcined at 900°C for 5 hours to produce CaO. X-ray fluorescence (XRF) analysis was carried out to evaluate the elemental composition of Pensi clam shells. The extracted CaO was used as a precursor to produce hydroxyapatite. The procedure used in the previous research was modified to synthesize hydroxyapatite. A total of 4.2 grams of finely calcined CaO powder, obtained from Pensi clam shells, was dissolved in 75 mL of 2M nitric acid

(HNO3). The resulting solution was stirred at 85°C and filtered. Subsequently, 250 mL of 0.18 M ammonium hydrogen phosphate ($(NH_4)_2HPO_4$) was added to the mixture in a dropwise manner, while it was agitated at a speed of 500 rpm and maintained at a temperature of 110°C. pH of the solution was raised to 11 by adding NH_4OH, and the mixture was constantly agitated for 5 hours. The precipitate and filtrate were separated after letting the produced white sol settle for the following day. The powder was heated for 5 hours at 110°C in an oven and then calcined for 3 hours at 800°C. The obtained hydroxyapatite sample was characterized using a variety of methods. The following equations represent the theoretical reactions involved in the synthesis of hydroxyapatite (Rahmayeni et al., 2023; Labanni et al., 2020).

$$CaCO_3 \rightarrow CaO + CO_2 \quad (1)$$

$$CaO + 2HNO_3 \rightarrow Ca(NO_3)_2 + H_2O \quad (2)$$

$$10Ca(NO_3)_2 + 6(NH_4)_3PO_4 + 2NH_4OH \rightarrow Ca_{10}(PO_4)_6(OH)_2 + 20NH_4NO_3 \quad (3)$$

2.4. Synthesis of Co-doped $ZnFe_2O_4$ with a mole ratio of Co:Zn of 0.1:0.9 ($Co_{0.1}Zn_{0.9}Fe_2O_4$)

$Co_{0.1}Zn_{0.9}Fe_2O_4$ nanoparticles were synthesized through the hydrothermal method using gambir leaf extract as a capping agent. For the synthesis, 8.079 g of $Fe(NO_3)_3{\cdot}9H_2O$, 2.353 g of $Zn(NO_3)_2{\cdot}6H_2O$, and 0.291 g of $Co(NO_3)_2$ were dissolved in 40 mL of a mixture comprising distilled water and gambir leaf extract in a 35:5 mL ratio. This solution was stirred at 500 rpm using a magnetic stirrer for 1 hour, after which 2M NaOH was added to adjust pH to 12. The resulting suspension was placed in an autoclave and heated at 180°C for 3 hours. The precipitate was filtered, washed with distilled water until pH became neutral, dried at 110°C for 3 hours, and then ground to a fine powder. The obtained $Co_{0.1}Zn_{0.9}Fe_2O_4$ powder was characterized using various instruments and subsequently used in the synthesis of nanocomposites (Rahmayeni et al., 2023).

2.5. Synthesis of HA/$Co_{0.1}Zn_{0.9}Fe_2O_4$

HA/$Co_{0.1}Zn_{0.9}Fe_2O_4$ nanocomposites were synthesized using the hydrothermal method. The procedure is as follows: First, HA and $Co_{0.1}Zn_{0.9}Fe_2O_4$ were mixed with a mole ratio of Co and Zn (0.1: 0.9) in 40 mL of gambir leaf extract and distilled water with a ratio of 5:35. The mixture was stirred until homogeneous for 30 minutes, then pH was adjusted to 12 by adding 2 M NaOH. The mixture's temperature was maintained in the range of 70°C – 80°C. Furthermore, the resulting suspension was heated at 180°C for 3 hours in an autoclave. The resulting brown precipitate was then filtered and washed with distilled water until a neutral pH of 7 was achieved. Furthermore, the precipitate was calcined at 400°C for 4 h. The obtained powder was dried at 110°C for 3 hours and then crushed until smooth. The Nanocomposite product was labeled as CoZnHA (Rahmayeni et al., 2023). The ratio effect of HA: $Co_{0.1}Zn_{0.9}Fe_2O_4$ was studied by synthesizing nanocomposite material into four variations based on the mass ratio of HA in HA/$Co_{0.1}Zn_{0.9}Fe_2O_4$ nanocomposites, as shown in Table 1. The proposed synthesis mechanism of nanocomposite is represented in Figure S1.

Table 1 Comparison of HA: $Co_{0.1}Zn_{0.9}Fe_2O_4$ and sample names

No.	Comparison of HA: $Co_{0.1}Zn_{0.9}Fe_2O_4$ (g)	Sample names CoZnHA
1	19 : 1	CoZnHA1
2	18 : 2	CoZnHA2
3	17 : 3	CoZnHA3
4	16 : 4	CoZnHA4

2.6. Characterization of samples

The synthesized samples were characterized using various analytical methods. X-ray diffraction (XRD: PANalytical MPD PW3040/60) with Cu Kα radiation in the range of 10-80° was used to determine the crystal structure. The morphology and elemental composition were examined using Scanning Electron Microscopy coupled with energy-dispersive X-ray Spectroscopy (SEM-EDX: HITACHI FLEXSEM 100). A more detailed analysis of structure, particle shape, and crystallinity

was carried out with TEM, HRTEM, and selected area electron diffraction (SAED) (TEM, JEM-1400). Fourier Transform Infrared Spectroscopy (FTIR: Subtech Spectrum ACII PEDS 4.00) was utilized to identify the interactions in the sample, with a wavenumber range of 200-4000 cm^{-1}. Magnetic properties were assessed using a Vibrating Sample Magnetometer (VSM, model VSM250). To analyze the absorption region and band gap energy, Diffuse Reflectance Spectroscopy UV-Vis (DRS-UV Vis SPECORD 210 Plus) was employed, while X-ray Photoelectron Spectroscopy (XPS: PHI-5702 multifunctional X-ray photoelectron spectrometer) measured the electron binding energies of the elements. Additionally, the pore size, surface area, and pore volume were determined using a Surface Area Analyzer (SAA: Quantachrome Nova 4200e). The quantity of reduced dye was quantified with a UV-Vis spectrophotometer (Thermo Scientific, Genesys 20), and the concentrations of adsorbed heavy metals were analyzed by Atomic Absorption Spectroscopy (AAS: AA240).

2.7. Photocatalytic activity determination of nanocomposites

The prior procedure was used to determine photocatalytic activity on the direct red 81 dye degradation (Rahmayeni et al., 2023). 10 mg of nanocomposites (CoZnHA1, CoZnHA2, CoZnHA3, and CoZnHA4) were added to 20 mL of a solution containing direct red 81 dye at a 30 mg/L concentration. After stirring, the resulting suspension was exposed to sunlight for 120 minutes, between 11:00 am and 1:00 pm. Following the irradiation, distilled water was added to restore the liquid to its initial volume. The suspension was then separated from the CoZnHA nanocomposite. Subsequently, aliquots were taken, and the absorbance was measured at 530 nm using a UV-Vis spectrophotometer. Photodegradation of the dye was measured by the following Equation 4:

$$D\ (\%) = \frac{A_0\text{-}A_t}{A_0}\ x\ 100\ \% \tag{4}$$

where A_o is the initial absorbance of the dye solution and At is the dye solution at a time in mn (Mohammed et al., 2024). The effect of several significant parameters-including catalyst types, dye concentration (10–50 mg/L), exposure time duration (30–120 minutes), and catalyst loading (0–25 mg)—on the photodegradation process was also examined. After the initial reaction cycles, the photocatalyst was retrieved, and the reusability was assessed by comparing it to a fresh sample, each experiment was repeated three times to test for repeatability.

2.8. Adsorption ability determination

The adsorption capacity of the synthesized samples for cadmium metal ions (Cd(II)) was evaluated using a modified version of the previous method (Sery et al., 2021). Nanocomposites selected for this assay are CoZnHA3 and CoZnHA4 due to their superior photocatalytic performance. The procedure carried out includes a stock solution of Cd(II) was first prepared by dissolving 1 g of $CdCl_2{\cdot}H_2O$ in distilled water in a 1000 mL volumetric flask, yielding a concentration of 1000 mg/L. Subsequently, cadmium ion solutions with concentrations of 20, 30, 40, and 50 mg/L were prepared by diluting the stock solution appropriately. The effect of initial concentration on the adsorption capacity of nanocomposite was assessed by adding 10 mg of nanocomposite to Cd(II) solutions of varying concentrations and allowing the mixtures to stand for 30 minutes. Subsequently, the liquid phase was separated from the nanocomposite solid using centrifugation, and the remaining cadmium ions that were not adsorbed were quantified using atomic absorption spectroscopy (AAS). The adsorption percentage was determined by comparing the metal ion concentrations before and after the treatment process. Equation 5 was applied to calculate the adsorption percentage for the tested samples.

$$\text{Adsorption percentage} = \frac{C_0\text{-}C_t}{C_0}\ \text{x}\ 100\% \tag{5}$$

Where C_0 is the initial concentration, and C_t is the final concentration of Cd(II) solution which is obtained using the Lambert-Beer equation (Kartika et al., 2023). The effect of the exposure time on the nanocomposite's adsorption capacity was investigated by adjusting the contact time (30, 60, 90, and 120 minutes). Additionally, variations in the amount of CoZnHA3 and CoZnHA4

nanocomposites (10, 15, 20, and 25 mg) were conducted to study the effect of adsorbent quantity on adsorption ability.

3. Results and Discussion

3.1. Structure analysis by XRD

To determine the crystallization properties and phase composition of synthesized samples XRD is studied. Figure 1(a) displayed the XRD pattern of standard $ZnFe_2O_4$, synthesized $ZnFe_2O_4$, and $Co_{0.1}Zn_{0.9}Fe_2O_4$. XRD pattern of the synthesized $ZnFe_2O_4$ sample exhibited the same pattern as ICSD standard #158837 with specific peaks at 2θ = 30.1˚, 35.7˚, 43.4˚, 53.7˚, 57.3˚ from the planes of (220), (311), (400), (422), and (511). The peaks were found to be well-defined with a good distribution of nanoparticles and crystalline nature, and no impurities were observed. Meanwhile, the $Co_{0.1}Zn_{0.9}Fe_2O_4$ pattern exhibited the same pattern as synthesized $ZnFe_2O_4$ with a slight shift of the peaks towards a larger 2θ, indicating a decrease in the lattice volume due to the smaller lattice parameters. The changes in 2θ are expected due to the substitution of a larger ionic cation, Zn^{2+} (radius of 0.82 Å), by a smaller Co^{2+} cation (radius of 0.74 Å). Equation 6 is Scherer's equation was used to estimate the average crystallite size for nanocomposites:

$$D = k\lambda / \beta \cos \theta \quad (6)$$

Where D represents the average crystallite size, λ denotes the wavelength of CuK radiation, β refers to the full width at half maximum (FWHM) of the diffraction peaks, θ is the Bragg angle, and K is the Scherrer constant (Suryawanshi et al., 2023). The average crystal size of $Co_{0.1}Zn_{0.9}Fe_2O_4$ is 10.18 nm. The small crystal size of $Co_{0.1}Zn_{0.9}Fe_2O_4$ is caused by the synthesis process using the hydrothermal method at a fairly low temperature, thereby the crystal growth is not perfect. The synthesis of spinel ferrite $CoxZn1\text{-}xFe_2O_4$ by other researchers employed the co-precipitation method, yielding crystal sizes between 24 to 40 nm. These larger crystal sizes, compared to those observed in this research, result from using the co-precipitation method followed by a high-temperature calcination process. Heating at elevated temperatures accelerates crystal growth by merging smaller crystals with identical orientations into larger ones (Asogekar and Verenkar, 2019).

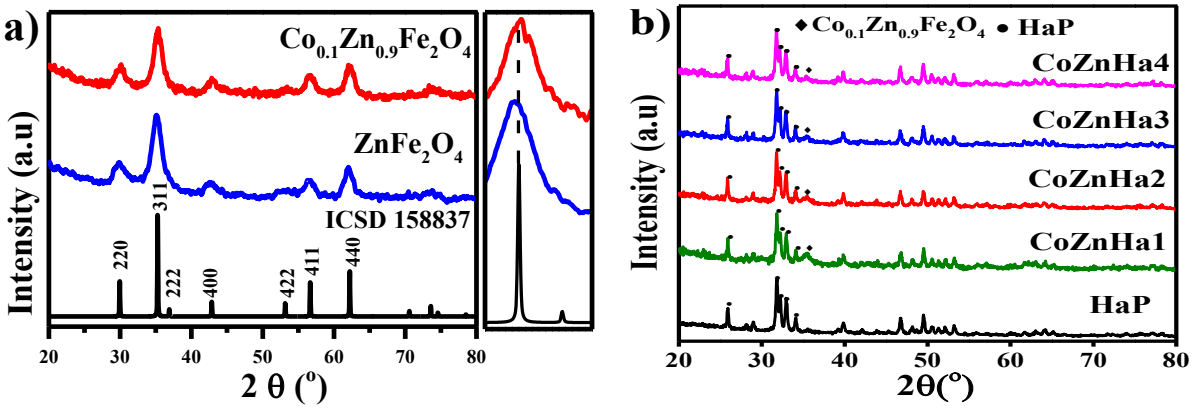

Figure 1 XRD a) patterns of standard $ZnFe_2O_4$, synthesized $ZnFe_2O_4$, and $Co_{0.1}Zn_{0.9}Fe_2O_4$, and b) composites

Figure 1(b) shows XRD patterns of hydroxyapatite samples and CoZnHA1, CoZnHA2, CoZnHA3, and CoZnHA4 nanocomposites. The diffractograms of nanocomposite samples show distinctive peaks for both hydroxyapatite and $Co_{0.1}Zn_{0.9}Fe_2O_4$, confirming the formation of nanocomposites. XRD patterns of synthesized nanocomposite exhibit the dominant peaks of the hydroxyapatite phase and a single peak of the $Co_{0.1}Zn_{0.9}Fe_2O_4$ phase with a lower intensity indicating the presence of both phases in nanocomposite samples. The specific diffraction peaks of $Co_{0.1}Zn_{0.9}Fe_2O_4$ were observed at 2θ = 35.9 with a Miller index (311), while the specific peaks of hydroxyapatite were observed at 2θ = 25.9˚, 31.8˚, 32.4˚, 33.9˚, 34.1˚, 39.8˚, 46.9˚, and 49.5˚.

Furthermore, no other peaks of any impurities and secondary phases are observed. The peak height of hydroxyapatite was not considerably impacted by the nanocomposite's increased mass of $Co_{0.1}Zn_{0.9}Fe_2O_4$.

3.2. Analysis by SEM-EDX

Figure 2 shows the morphology of the CoZnHA nanocomposite analyzed by SEM with a magnification of 20,000. Hydroxyapatite granules exhibit a relatively homogenous shape with slight agglomeration. The capping agent used can affect the morphology forms.

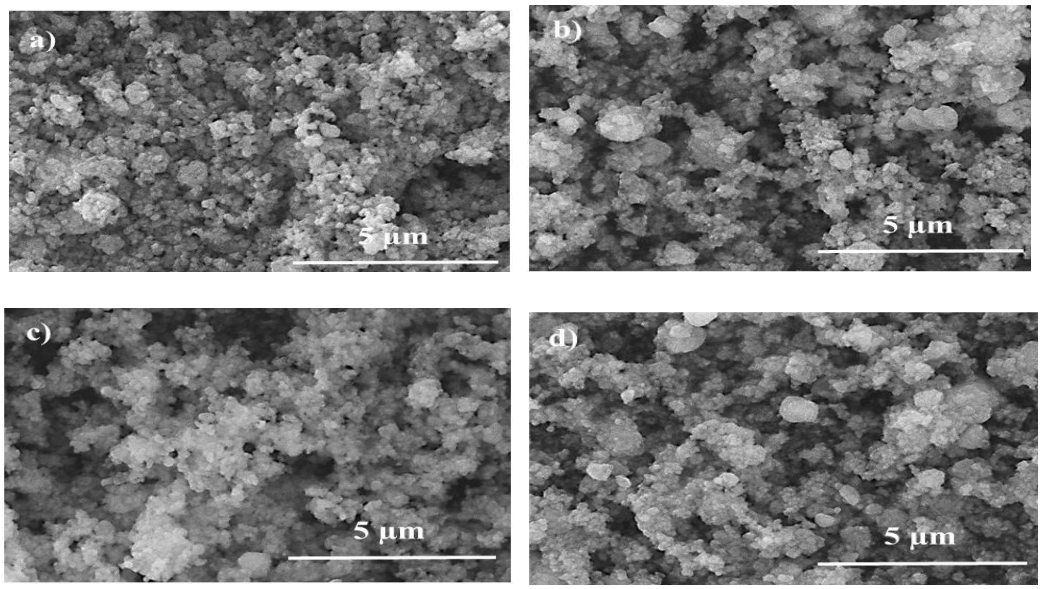

Figure 2 SEM images of a) CoZnHA1, b) CoZnHA2, c) CoZnHA3, and d) CoZnHA4 with magnification of 20,000

In this research, gambir leaf extract was used as a source of capping agent due to gambir leaf extract containing secondary metabolite compounds such as flavonoids, which can act as a capping agent. The presence of a capping agent in gambir leaf extract can minimize the occurrence of agglomeration (Wahyuni et al., 2019). Since spinel ferrite's magnetic characteristics attract each other to create larger clusters, adding more spinel ferrite results in a slightly agglomerated nanocomposite.

The components of the nanocomposite were examined using an EDX device. Figure S2 shows the EDX spectrum of CoZnHA, illustrating the elements present in nanocomposite samples. The elements present in CoZnHA nanocomposite, such as calcium (Ca), phosphate (P), and oxygen (O), which are constituent elements of hydroxyapatite, cobalt (Co), iron (Fe), and zinc (Zn), which are constituent elements of $Co_{0.1}Zn_{0.9}Fe_2O_4$, are indicated by the peaks that appear in EDX spectrum. CoZnHA nanocomposite contains a more significant Ca and P element composition than the pristine $Co_{0.1}Zn_{0.9}Fe_2O_4$ because hydroxyapatite is a matrix and exists in a greater quantity. The increase in the ferrite content in the nanocomposite is directly proportional to the height of the peaks representing the ferrite's constituent elements (Table 2).

Table 2 Composition of elements in the synthesized composites

No.	Elements (%w)	CoZnHA1	CoZnHA2	CoZnHA3	CoZnHA4
1	Co	0.41	0.36	0.41	0.69
2	Fe	2.88	4.73	6.04	9.91
3	O	39.61	37.8	40.73	38.33
4	Zn	1.57	1.85	2.51	4.11
5	Ca	35.56	37.10	33.5	30.38
6	P	19.64	18.67	16.81	16.58

3.3. Analysis by TEM, HRTEM, and SAED

A more detailed analysis of structure, particle shape, and crystallinity was carried out with TEM, HRTEM, and selected area electron diffraction (SAED) (Figure 3). TEM image of $Co_{0.1}Zn_{0.9}Fe_2O_4$ (Figure 3a–b) illustrates the particles' morphology in the cube-like granular phase with diameters less than 50 nm.

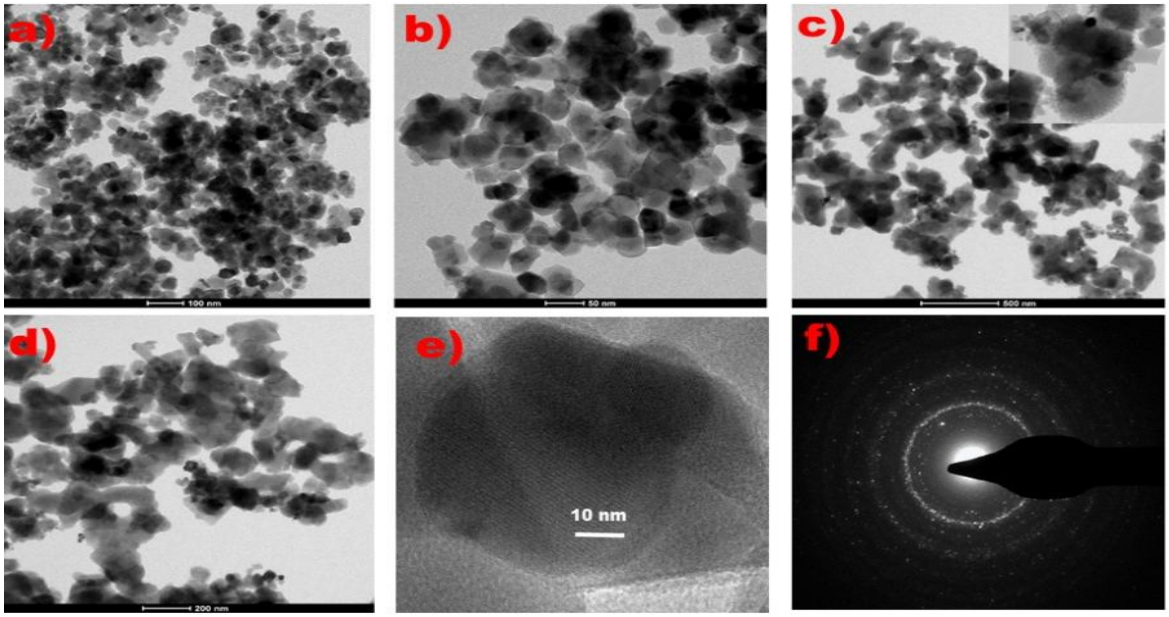

Figure 3 TEM images of $Co_{0.1}Zn_{0.9}Fe_2O_4$ with different magnifications (a-b), CoZnHA3 and CoZnHA4 nanocomposites (c-d), HRTEM image and SAED pattern of CoZnHA4 (e-f)

There is a slight agglomeration caused by the magnetic properties of the spinel ferrite in nanocomposites. Figure 3(c-d) illustrates the granular morphology of CoZnHA3 and CoZnHA4 nanocomposite particles, where $Co_{0.1}Zn_{0.9}Fe_2O_4$ ferrite spinel is encapsulated in hydroxyapatite. Figure 3e presents the HRTEM image of the CoZnHA4 nanocomposite, indicating that the combined components are on the nanoscale. SAED patterns shown in Figure 3f show the polycrystalline nature of the samples under investigation. The ring pattern is indexed to reflections corresponding to the Fd-3m space group. Moreover, SAED patterns closely match the simulated patterns generated from ferrite crystal structure data. Compared to previous investigations that used $CuFe_2O_4$ as the ferrite material, nanocomposite particles produced in this research exhibit a more uniform and regular shape (Rahmayeni et al., 2023).

3.4. Analysis by FTIR

FTIR spectroscopy was utilized to validate the spinel ferrite and hydroxyapatite structures in the prepared samples. Figure 4 shows FTIR spectroscopy of prepared samples in the range from 400 to 2000 cm^{-1}. Figure 4a shows the band of hydroxyapatite and $Co_{0.1}Zn_{0.9}Fe_2O_4$.

The specific absorption band of $Co_{0.1}Zn_{0.9}Fe_2O_4$ appeared at a wave number of 482 cm^{-1}, which indicates the presence of M–O vibrations on the octahedral side of Fe-O/Co-O, while the absorption at a wave number of 534 cm^{-1} indicates the presence of M–O vibrations on the tetrahedral side of Zn-O/Co-O. The bands observed in this investigation are consistent with previous results (Mohamed et al., 2019). Meanwhile, the spectrum of hydroxyapatite appeared at specific wave numbers of 564 cm^{-1} and 597 cm^{-1}, which indicates the antisymmetric vibration of the O-P-O bond from the PO_4^{3-} group (Sery et al., 2021). Additionally, the FTIR spectrum of the synthesized CoZnHA (1-4) nanocomposites is shown in Figure 4b. The absorption band at 1018 cm^{-1} corresponds to the PO_4^{3-} group from hydroxyapatite, while the band at 1628 cm^{-1} is attributed to the C=C group (alkene) from the betel leaf extract. Moreover, the absorption below 548 cm^{-1} indicates the Fe-O stretching vibration of the ferrite spinel in nanocomposites (Cahyana et al., 2021).

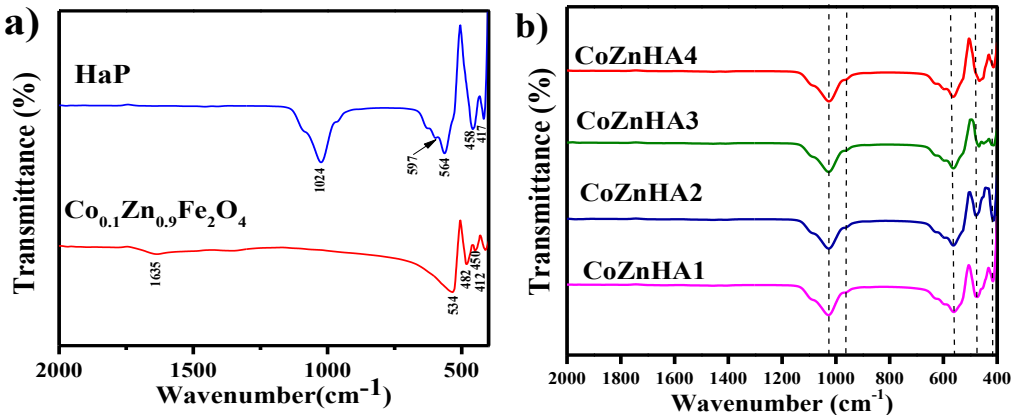

Figure 4 FTIR spectroscopy of $Co_{0.1}Zn_{0.9}Fe_2O_4$ and hydroxyapatite (a) and CoZnHA1, CoZnHA2 CoZnHA3, and CoZnHA4 (b)

3.5. Magnetic properties analysis by VSM

Magnetic properties of synthesized nanocomposites with different ratios of hydroxyapatite and $Co_{0.1}Zn_{0.9}Fe_2O_4$ were investigated using VSM equipment at room temperature, which is given in the form of hysteresis curve, as shown in Figure 5A.

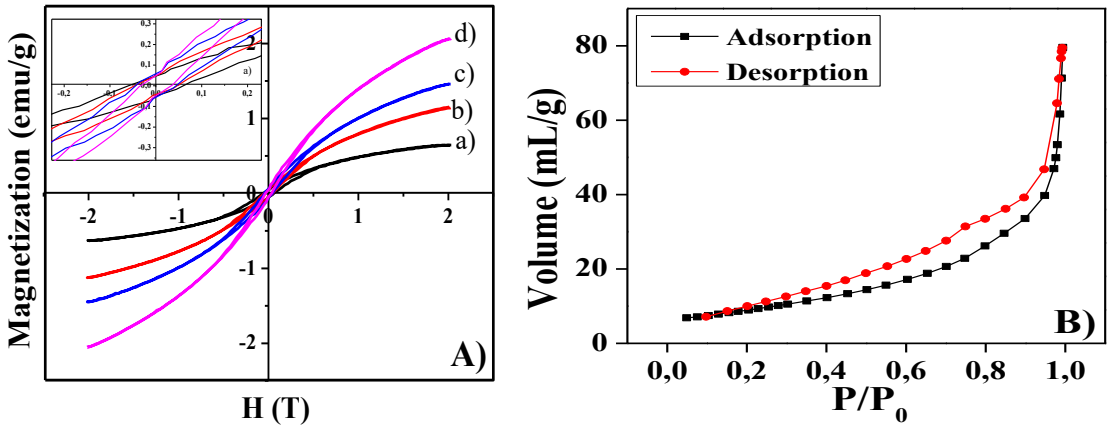

Figure 5 A) Hysteresis curve of a) CoZnHA1, b) CoZnHA2, c) CoZnHA3, d) CoZnHA4, and B) N_2 adsorption-desorption isotherm curve for CoZnHA4 sample

The hysteresis curve indicates that nanocomposite samples exhibit soft magnetic properties, as evidenced by the relatively low values of saturation magnetization (Ms), remanent magnetization (Mr), and coercivity (Hc) for nanocomposites, as presented in Table 3. The magnetic properties of nanocomposites are attributed to $Co_{0.1}Zn_{0.9}Fe_2O_4$, as hydroxyapatite is not a magnetic material. Consequently, the magnetic properties of nanocomposite enhance with the increasing amount of ferrite. According to Das and Dhar (2020a), the small Ms value occurs due to the coating of non-magnetic materials, such as hydroxyapatite, on magnetic material in nanocomposites (Das et al., 2021).

Table 3 Saturation magnetic (Ms), remanent magnetic (Mr), and coercivity (Hc) values of the synthesized nanocomposite samples

No.	Samples	Ms (emu/g)	Mr (emu/g)	Hc (Oe)	Mr/Ms
1.	CoZnHA1	0.6424	0.0467	59.6	0.073
2.	CoZnHA2	1.1365	0,0486	44.2	0.043
3.	CoZnHA3	1.4587	0.0490	44.2	0.033
4.	CoZnHA4	2.0681	0.0582	33.5	0.028

From the shape of the hysteresis curve, it can be concluded that CoZnHA nanocomposites are superparamagnetic following the research results obtained by Gómez et al. (2018). The magnetic properties of the obtained nanocomposites are stronger than those obtained by Das and Dhar (2020a) and Rahmayeni et al. (2023). Magnetic property of nanocomposites are an advantage of the catalyst in a photocatalytic degradation process. These nanocomposites can be separated from the solution quickly and easily with a permanent magnet after the degradation photocatalytic process and can be used for the next application (Ai et al., 2023).

3.6. Adsorption-desorption analysis by BET

Figure 5B shows the adsorption-desorption isotherm curve from Brunauer-Emmett-Teller (BET) analysis for the CoZnHA4 nanocomposite. The curve indicates a gradual increase in relative pressure (P/P0) initially, but a rapid increase is observed at a relative pressure range of 0.6 to 1. The increase in P/P0 is due to the interaction of adsorbed gas molecules on the surface of the solid, forming a single layer (Kahrizi et al., 2018). CoZnHA4 sample has an average pore diameter of 7.52 nm, placing it in the mesoporous category, as mesopores range from 2 to 50 nm. The specific surface area of the CoZnHA4 sample is 32.01 m^2/g, and its pore volume is 0.12 mL/g. The results obtained are broader than those reported in previous research (Ullah et al., 2023). It is well established that surface area plays a critical role in determining a material's effectiveness as both a photocatalyst and an adsorbent. A larger surface area provides more active sites for interactions with dyes and metal ions, leading to higher activity.

3.7. Optical properties analysis by DRS-UV Vis

The optical properties of nanocomposite samples were evaluated using DRS UV-Vis equipment. The Kubelka-Munk theory, which is commonly used for analyzing optical band gap energy through diffuse reflectance, was utilized in this research (Paydar et al., 2020).

Using the Tauc equation, the estimated band gap energy of each nanocomposite was 2.4, 2.35, 2.31, and 2.4 eV for CoZnHA1, CoZnHA2, CoZnHA3, and CoZnHA4, respectively (Figure 6). The band gap variation depends on various factors such as crystallite size, crystallinity, lattice strain, structural parameters, and the presence of defects or impurities (Yadav et al., 2017). The increment of the optical band gap energies by increasing the $Co_{0.1}Zn_{0.9}Fe_2O_4$ proportion from 5 wt% to 20 wt% (decrement of HA proportion from 95 wt% to 80 wt%). The measured band gap energy indicates that CoZnHA nanocomposite absorbs light in the visible region, which is relevant in this research as sunlight was used as the light source (Das et al., 2021). This optical property is helpful in its application as a photocatalyst because sunlight can move its activity to degrade organic dyes more efficiently.

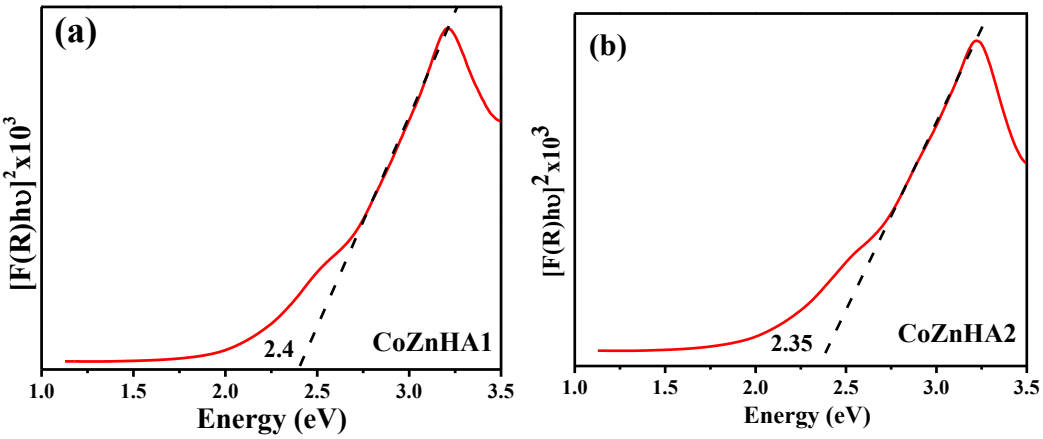

Figure 6 The Tauc Plot of CoZnHA1 (a), CoZnHA2 (b), CoZnHA3 (c), and CoZnHA4 (d) to estimate the energy gap obtained from DRS UV-vis measurements

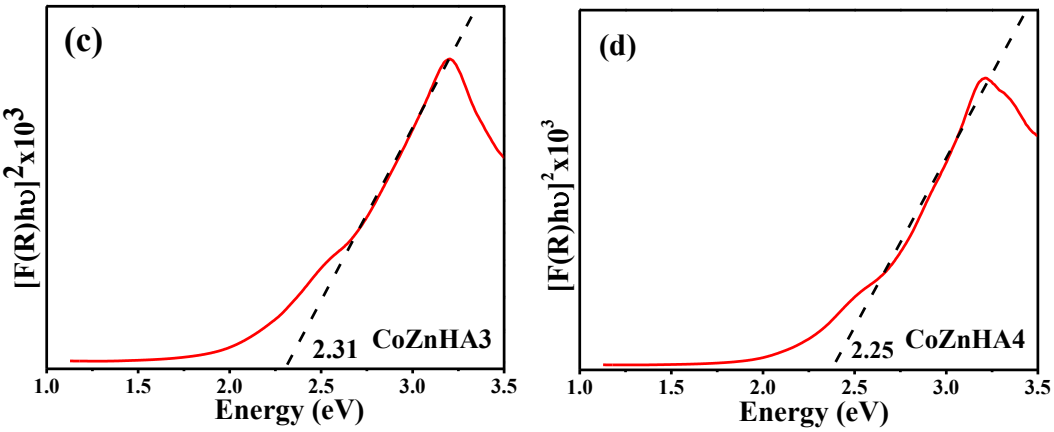

Figure 6 The Tauc Plot of CoZnHA1 (a), CoZnHA2 (b), CoZnHA3 (c), and CoZnHA4 (d) to estimate the energy gap obtained from DRS UV-vis measurements (Cont.)

3.8. XPS research

X-ray photoelectron spectroscopy (XPS) was utilized to investigate the elemental composition and electron states of atoms in the material (Figure S3). XPS spectrum provided comprehensive details on the surface composition and chemical states of all elements present in CoZnHA4. The high-resolution XPS spectra of CoZnHA4 (Figure S3a) and the spectra for O1s, Ca2p, P2p, C1s, Fe2p, Zn2p, and Co2p are displayed in Figures S3b–f. XPS spectrum of O 1s indicates the presence of various oxygen species on the sample's surface. In Figure S3b, the peak at 527.7 eV ($O1s_{3/2}$) is assigned to lattice oxygen (M–O–M) in the metal-oxygen framework, while the peak at 530 eV (O $2p_{1/2}$) corresponds to oxygen atoms in PO_4^{3-} group. The high-resolution XPS spectrum for Ca2p, shown in Figure S3c, reveals two peaks with binding energies of 349.3 eV (Ca $2p_{1/2}$) and 345.7 eV (Ca $2p_{3/2}$).

The peak around 349.2 eV for Ca $2p_{3/2}$ indicates that calcium atoms are bonded to phosphate groups (PO_4^{3-}). In Figure S3d, the P2p spectrum shows two peaks at binding energies of 131.6 eV (P $2p_{1/2}$) and 132.1 eV (P $2p_{3/2}$) in the nanocomposite. These binding energy values for P2p are lower than those typically found in pure hydroxyapatite (134.13 eV and 133.18 eV), suggesting an interaction with $Co_{0.1}Zn_{0.9}Fe_2O_4$ nanoparticles (Das and Dhar, 2020a). In the arrangement of oxygen atoms, Fe(II) is positioned at the octahedral site, while Fe(III) occupies the tetrahedral site. The deconvoluted iron peak reveals two primary peaks with binding energies of 709.04 eV and 723.36 eV, corresponding to $Fe2p_{3/2}$ and $Fe2p_{1/2}$, respectively (Figure S3e). Zn 2p core-level spectra, shown in Figure S3f, display two fitting peaks at approximately 1018.7 eV and 1042 eV, which are attributed to Zn $2p_{3/2}$ and Zn $2p_{1/2}$, respectively (Hanamanta et al., 2023). The appearance of these element peaks indicates the formation of hydroxyapatite/ $Co_{0.1}Zn_{0.9}Fe_2O_4$ nanocomposite. C 1s peak observed at 283 eV is predicted to be the carbon used in the measurements (Figure S3h).

3.9. Photocatalytic activity

Photocatalytic activity of nanocomposite was determined by the degradation of direct red 81 dye under direct solar light (Figure 7). To obtain nanocomposites with higher activity, photocatalytic activity was determined for all nanocomposites using direct red 81 dye solution with the following conditions: the dye concentration is 20 mg/L, the amount of nanocomposite is 20 mg, and the exposure time is 2 h. From Figure 7a, it can be seen that without a catalyst (NC), the degradation percentage only reaches 28%. With a catalyst in the form of a composite, the degradation percentage increases above 80%. CoZnHA3 and CoZnHA4 nanocomposites exhibit better activity compared to the other nanocomposites. Therefore, CoZnHA3 and CoZnHA4 were utilized to determine the optimal concentration and contact time. The efficiency test for direct red 81 dye concentration revealed a degradation percentage of 92.25% after 2 hours (Figure 7b). As the concentration

increases, the degradation percentage obtained becomes lower. The decrease in degradation percentage with increasing dye concentration is due to the higher number of direct red 81 molecules in the liquid, which blocks sunlight from reaching nanocomposite material. Consequently, OH· formation, which is crucial for the degradation process, is reduced. According to reports, OH radical is a group that plays an important role in breaking down dye compounds into CO_2 and H_2O (Kusdianto et al., 2020). This result is consistent with the results reported by Das and Dhar (2020a). In this photocatalytic process, the presence of hydroxyapatite in the composite can help spread the ferrite material, thereby agglomeration can be reduced and catalytic activity becomes better.

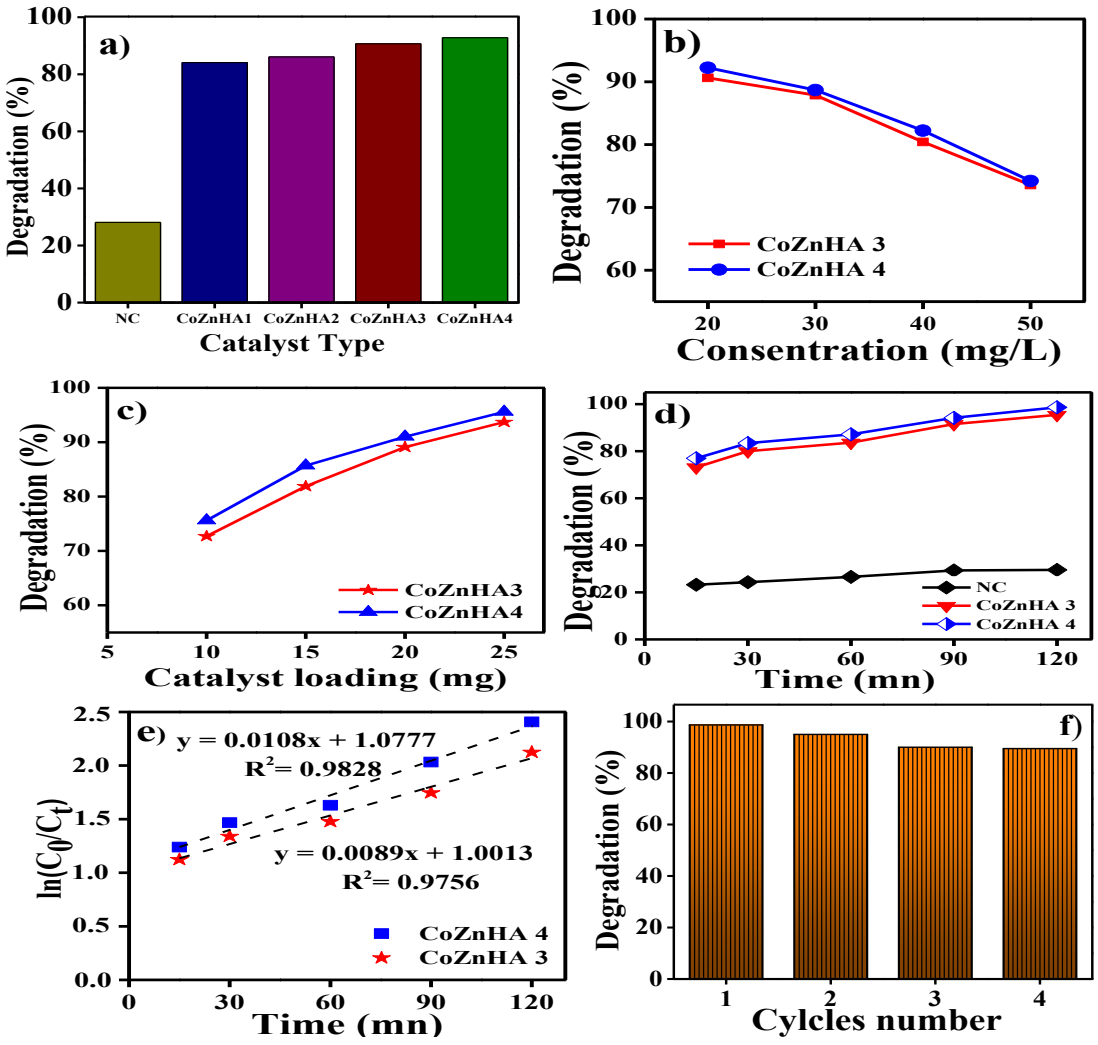

Figure 7 Photocatalytic activity of samples (a) with different concentrations of direct red 81 concentrations, (b) with different amounts of CoZnHA catalyst, (c) with different exposure times, (d) the reaction kinetics in the degradation of direct red 81 dye, and (f) recycles number

The determination of the optimal dosages of nanocomposites used as photocatalysts in the degradation of direct red 81 dye is shown in Figure 7c. The degradation percentage increases with the number of photocatalysts as more active sites become available for the degradation process. The optimal photocatalyst dosage is 25 mg, resulting in a degradation percentage of 95.57%. According to reports by Rahmayeni et al. (2022), increasing the amount of photocatalyst provides more active sites, leading to improved dye degradation. The best exposure contact time test for CoZnHA nanocomposite on direct red 81 dye degradation is shown in Figure 7d. The optimal contact time was found to be 2 hours, with the degradation percentage reaching 98,65%. Rahmayeni et al.'s research indicates that the proportion of degradation increased with exposure duration. With the

increasing contact time, the degradation efficiency increased because the number of OH· radicals formed increased (Rafiq et al., 2021; Rahmayeni et al., 2019).

The kinetic parameters were determined by plotting ln(Ct/C0) against the reaction time. Figure 7e is the reaction kinetics curve in the photocatalysis process driven by sunlight. From the shape of the curve, it can be concluded that the kinetics of the degradation process follow the pseudo-first-order kinetic model (Hassaan et al., 2022). The recycling test of CoZnHA4 nanocomposite was conducted by separating the photocatalyst after each cycle of exposure using centrifugation to recover the catalyst. The recovered catalyst was then washed with absolute alcohol, followed by deionized water. It was subsequently dried overnight in an oven at 70°C. After drying, the collected nanocatalyst was reintroduced into a freshly prepared direct red 81 dye solution to begin the next experimental cycle (Figure 7f). In the first and second cycles, there was a slight decrease in degradation percentage. However, in cycles 3 and 4, the reduction in degradation percentage was not significant.

3.10. Adsorption ability determination of Cd(II) ion in water

The heavy metal Cd(II) in water was used to test the nanocomposite capacity for adsorption (Figure 8). The effect of initial concentration on the removal of Cd(II) ions by CoZnHA3 and CoZnHA4 adsorbents was investigated at different initial concentrations ranging from 20 to 50 mg/L. Figure 8a presents the curve demonstrating the composite capability to adsorb Cd(II) metal ions at various concentrations. Initially, the adsorption capacity increased with the rise in the initial dye concentration. This can be attributed to the fact that at lower initial concentrations, the adsorbent surface is more accessible. As the initial concentration of Cd(II) increases, the number of Cd(II) metal ions adsorbed also increases. However, once all active sites on the adsorbent are occupied, further increases in Cd(II) concentration result in a decrease in adsorption capacity due to the lack of available adsorption sites. The optimum metal ion concentration obtained was 20 mg/L with an adsorption percentage of 90.9 % and 92.51% for CoZnHA3 and CoZnHA4. According to Das and Dhar (2020b), increasing the concentration of Cd(II) ions will reduce the adsorption efficiency because the amount of adsorbent that remains is not proportional to the greater number of Cd(II) ions, thereby the adsorbent has reached a saturation point in its adsorption. Moreover, the saturation of the active site leads the dye molecules to be released back into the solution due to the agitation (Rahmayeni et al., 2023; Das and Dhar, 2020b).

To investigate the impact of adsorbent quantity, 10 to 30 mg of nanocomposite was used keeping the other parameters. The result showed that, at an initial metal concentration of 30 mg/L, the maximum removal percentage of Cd(II) for the adsorbent dosage of 25 mg was around 78.05% and 81.09% for CoZnHA3 and CoZnHA4 (Figure 8b). It was observed that increasing the amount of nanocomposite led to higher adsorption efficiency, as more active sites on the composite surface became available to adsorb Cd(II) metal ions (Nayak and Bhushan, 2021).

Furthermore, contact time also plays a role in adsorption efficiency. The time-dependent behavior of Cd(II) adsorption was assessed by varying the contact time between the adsorbate and adsorbent from 15 to 120 minutes, using an initial concentration of 30 mg/L and 25 mg of adsorbent. CoZnHA3 and CoZnHA4 nanocomposites were used for this study. The graph shows that the adsorption grew quickly during the first 60 mn before becoming slowly saturated at the 120-minute mark (Figure 8c). During the initial stage of adsorption, a larger number of active sites are available on the adsorbent. However, as contact time increases, these active sites gradually become occupied, leading to a decrease in the number of available sites. This results in a slower adsorption rate until equilibrium is eventually reached (Hassaan et al., 2022; Nayak and Bhushan, 2021). The optimum contact time for Cd(II) metal ions adsorption is 120 mn with an adsorption percentage of 88.99%. The adsorption capacity for 2 hours was 97.3 mg/g for CoZnHA3 and 97.9 mg/g for CoZnHA3.

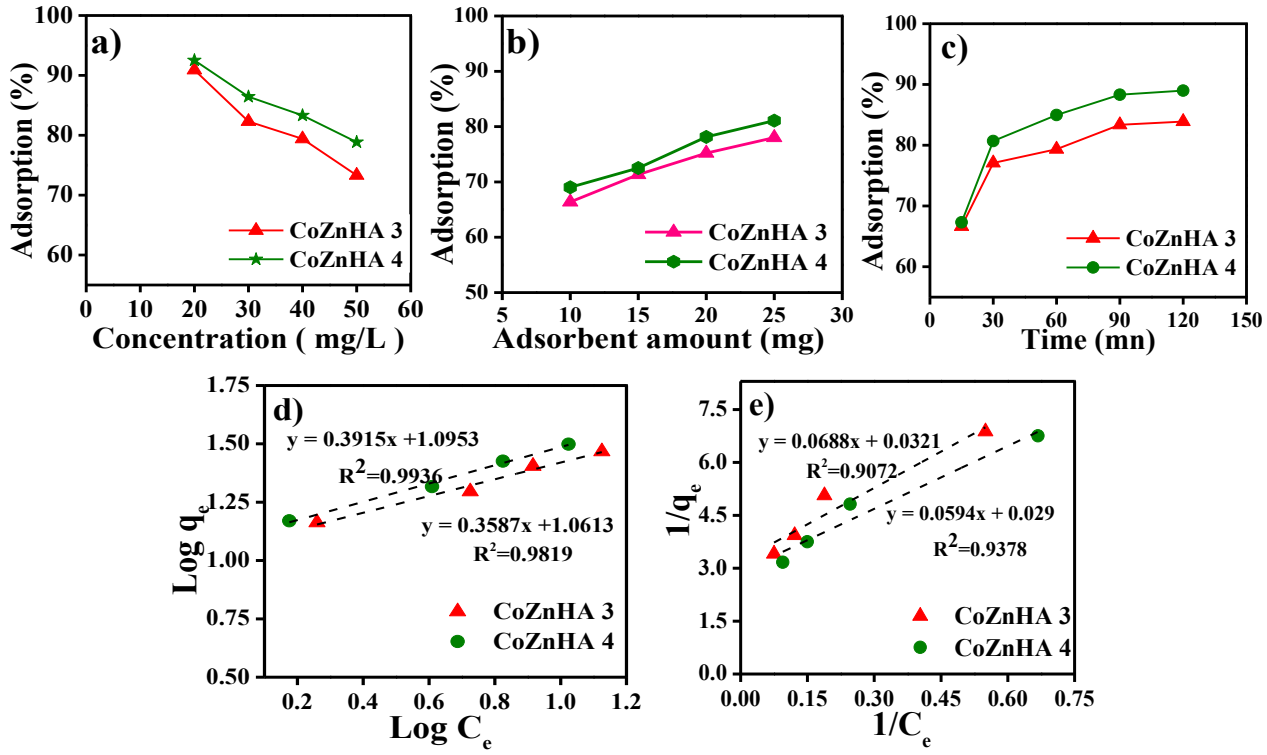

Figure 8 Test graph for nanocomposite adsorption capability (a) variation in the amount of CoZnHA adsorbent (b) variation in CoZnHA adsorption time, (c) variation in Cd(II) metal ion concentration, and (d) Freundlich isotherm curve, and (e) Langmuir isotherm curve of Cd(II) ion adsorption

Adsorption isotherms were evaluated using Langmuir and Freundlich models. Langmuir isotherm refers to an adsorption process that takes place chemically in a single layer (monolayer), while Freundlich isotherm refers to a chemical adsorption process that involves many layers (multilayer). The linear form of the Langmuir and Freundlich equation can be expressed in Equations 7 and 8, as follows:

$$\frac{C_e}{q_e} = \frac{C_e}{q_m} + \frac{1}{q_m K_L} \quad \text{Langmuir} \tag{7}$$

$$\ln q_e = \ln K_F + \frac{1}{n} \ln C_e \quad \text{Freundlich} \tag{8}$$

In this context, q_e (mg/g) represents the equilibrium concentration of metal ions, C_e (mg/L) denotes the equilibrium adsorption concentration for Cd(II), and q_m (mg/g) indicates the maximum adsorption capacity. K_L is the adsorption constant of the Langmuir model. The constants b and q_m can be determined from the slope and intercept of the linear plot of 1/qe versus 1/Ce . K_F represents the adsorption constant of the Freundlich model. n was the Freundlich isotherm exponent (Wang and Shih, 2021; Wang et al., 2019). The Freundlich isotherm was obtained by graphing Log Ce vs log qe (Figure 8d) and the Langmuir model on the equilibrium data was obtained by plots of 1/Ce versus 1/Qe (Figure 8e).

Table 4 Langmuir and Freundlich isotherm coefficients for the adsorption of Cd(II) ion

No.	Adsorbent	Langmuir isotherm			Freundlich isotherm		
		K_L (L/mg)	Q_m (mg/g)	R^2	K_F	n	R^2
1.	CoZnHA 3	0.46	97.3	0.9072	1.077	14.53	0.9936
2.	CoZnHA 4	0.49	97.9	0.9378	1.069	16.84	0.9819

The results of the isotherm analysis are summarized in Table 4. By comparing the coefficient of determination (R^2), it is evident that the Langmuir isotherm model was not suitable for this research. The adsorption kinetics of Cd (II) ions were found to follow the Freundlich isotherm model, with

R^2 values of 0.9936 for CoZnHA3 and 0.9819 for CoZnHA4. The maximum capacity obtained from Langmuir isotherm using CoZnHA 4 adsorbent is 97.9 mg/g. The maximum capacity obtained in this research was lower than the results obtained by several previous research (Table 5). This difference may be due to the smaller amount of adsorbent used, variations in experimental conditions, and differences in the type of adsorbent.

Table 5 Maximum adsorption capacity of different adsorbents for Cd(II) ions removal

No.	Material	Capacity (mg/g)	References
1.	$NiFe_2O_4$/HAp/graphene	344.83	(Kahrizi et al., 2018)
2.	Magnetic ferrite	160	(Liu et al., 2018)
3.	HAP/$ZnFe_2O_4$	107	(Das and Dhar, 2020b)
4.	$xZnO_{(1-x)}Fe_2O_4$	82.45	(Khezami et al., 2017)
5.	Hydroxyapatite/$Co_{0.1}Zn_{0.9}Fe_2O_4$	97.9	This work

4. Conclusions

Magnetic hydroxyapatite/$Co_{0.1}Zn_{0.9}Fe_2O_4$ nanocomposites were successfully synthesized using Pensi clam shells as a source of CaO, which was then utilized to prepare hydroxyapatite. X-ray analysis reveals that the nanocomposites exhibit good crystallinity without impurities. Absorption bands at wave numbers 482 and 534 cm^{-1} indicated the presence of octahedral and tetrahedral sites of spinel ferrite in the nanocomposite. The magnetic properties of the samples increase with decreasing amounts of hydroxyapatite and growing quantities of spinel ferrite in the composite, as shown by the magnetic saturation value. HA/$Co_{0.1}Zn_{0.9}Fe_2O_4$ nanocomposites presented an efficient and environmentally friendly method for removing heavy metals and dyes from wastewater. Under optimal conditions, the catalytic activity of nanocomposite achieved 98.65% degradation of direct red 81 dyes after two hours driven by sunlight irradiation. This removed 92.51% of Cd(II) ions from the aqueous solution, and the maximum capacity obtained from Langmuir isotherm using CoZnHA 4 adsorbent was 97.9 mg/g. Furthermore, the nanocomposite exhibited sufficient magnetic strength, enabling its easy isolation from the reaction mixture using an external magnet. Therefore, nanocomposites function as magnetically separable and highly recyclable catalysts for the degradation of pollutant dyes and metal ions in contaminated water.

Acknowledgements

The authors are grateful to the Ministry of Education, Culture, Research, and Technology of Indonesia for funding under Research Contract Number DRTPM: 012/E5/PG.02.00.PL/2023, and Unand: T/15/UN16.19/PT.01.03/PDUPT-Material Maju/2023.

Author Contributions

RY – conceptualization, supervision, experiment and analysis; RF – Experiment & Investigation; ZF – Analysis, writing & review; TPW - Editing & review; YS - Analysis, Editing & review; ZH - Formal analysis; – Review.

Conflict of Interest

The authors declare no competing interests.

References

Ai, J, Shuai, Y, Hu, M, Cheng, L, Luo, S, Li, W, Chen, Z, Hu, L & Zhou, Z 2023, 'Microstructural evolution and catalytic properties of novel high-entropy spinel ferrites MFe_2O_4 (M= Mg, Co, Ni, Cu, Zn)', *Ceramics International*, vol. 49, pp. 22941–22951, https://doi.org/10.1016/j.ceramint.2023.04.119

Asogekar, PA & Verenkar, VMS 2019, 'Structural and magnetic properties of nanosized $Co_xZn(1-x)Fe_2O_4$ (x= 0.0, 0.5, 1.0) synthesized via autocatalytic thermal decomposition of hydrazinated cobalt zinc ferrous succinate', *Ceramics International*, vol. 45, pp. 21793–21803, https://doi.org/10.1016/j.ceramint.2019.07.182

Cahyana, AH, Liandi, AR, Yulizar, Y, Romdoni, Y & Wendari, TP 2021, 'Green synthesis of CuFe2O4 nanoparticles mediated by Morus alba L. leaf extract: Crystal structure, grain morphology, particle size, magnetic and catalytic properties in Mannich reaction', *Ceramics International*, vol. 47, pp. 21373–21380, https://doi.org/10.1016/j.ceramint.2021.04.146

Das, KC & Dhar, SS 2020a, 'Remarkable catalytic degradation of malachite green by zinc supported on hydroxyapatite encapsulated magnesium ferrite ($Zn/HAP/MgFe_2O_4$) magnetic novel nanocomposite', *Journal of Materials Science*, vol. 55, pp. 4592–4606, https://doi.org/10.1007/s10853-019-04294-x

Das, KC & Dhar, SS 2020b, 'Removal of cadmium(II) from aqueous solution by hydroxyapatite-encapsulated zinc ferrite ($HAP/ZnFe_2O_4$) nanocomposite: Kinetics and isotherm study', *Environmental Science and Pollution Research*, vol. 27, pp. 37977–37988, https://doi.org/10.1007/s11356-020-09832-8

Das, KC, Dhar, SS, Thakurata, DG & Das, J 2021, 'Sn(II) inserted on hydroxyapatite encapsulated nickel ferrite ($NiFe_2O_4$@HAp-Sn^{2+}): A novel nanocomposite for the effective photo-degradation of rhodamine B dye', *Journal of Cleaner Production*, vol. 290, pp. 1–12, https://doi.org/10.1016/j.jclepro.2020.125172

Dehghani, M, Ahmadi, B, Zonnoon, Y, Nourozi, E & Shamsedini, N 2018, 'Decolorization of Direct Red 81 in aqueous solutions by Fenton oxidation process: Effect of system parameters', *Iranian Journal of Health, Safety and Environment*, vol. 6, pp. 1297–1302

Desalegn, YM, Andoshe, DM & Desissa, TD 2020, 'Composite of bentonite/CoFe2O4/hydroxyapatite for adsorption of Pb (II)', *Materials Research Express*, vol. 7, article 11, https://doi.org/10.1088/2053-1591/abc71f

Elgarahy, AM, Elwakeel, KZ, Mohammad, SH & Elshoubaky, GA 2021, 'A critical review of biosorption of dyes, heavy metals and metalloids from wastewater as an efficient and green process', *Cleaner Engineering and Technology*, vol. 4, article 100209, https://doi.org/10.1016/j.clet.2021.100209

Fatah, AFMA, Mohamad, AA, Ali, SAM, Muchtar, A, Arifin, NA, Wan Yusoff, WNA & Hamid, NA 2023, 'Influence of ZnO on electrochemical and physiochemical properties of lanthanum strontium cobalt ferrite as cathode for intermediate temperature solid oxide fuel cells', *International Journal of Technology*, vol. 14, no. 5, pp. 1123–1133, https://doi.org/10.14716/ijtech.v14i5.6341

Ganesan, M, Ganapathi, B & Govindasamy, P 2024, 'CoFe2O4/rGO nanocomposite: Synthesis and enhanced ammonia gas sensing properties at room temperature', *Results in Chemistry*, vol. 7, pp. 2-7, https://doi.org/10.1016/j.rechem.2024.101342

Gómez-Polo, C, Recarte, V, Cervera, L, Beato-López, JJ, López-García, J, Rodríguez-Velamazán, JA, Ugarte, MD, Mendonça, EC & Duque, JGS 2018, 'Tailoring the structural and magnetic properties of Co-Zn nanosized ferrites for hyperthermia applications', *Journal of Magnetism and Magnetic Materials*, vol. 465, pp. 211-219, https://doi.org/10.1016/j.jmmm.2018.05.051

Hanamanta, Matteppanavar, S & Hegde, BG 2023, 'Magnetic and electrical investigations of low dimensional $Co_{0.5}Zn_{0.5-x}Cu_xFe_2O_4$ nano ferrites', *Journal of Alloys and Compounds*, vol. 954, article 170031, https://doi.org/10.1016/j.jallcom.2023.170031

Handayani, T, Emriadi, Deswati, Ramadhani, P & Zein, R 2024, 'Modelling studies of methylene blue dye removal using activated corn husk waste: Isotherm, kinetic and thermodynamic evaluation', *South African Journal of Chemical Engineering*, vol. 47, pp. 15-27, https://doi.org/10.1016/j.sajce.2023.10.003

Hassaan, MA, El Nemr, A, El-Zahhar, AA, Idris, AM, Alghamdi, MM, Sahlabji, T & Said, TO 2022, 'Degradation mechanism of Direct Red 23 dye by advanced oxidation processes: A comparative study', *Toxin Reviews*, vol. 41, pp. 38-47, https://doi.org/10.1080/15569543.2020.1827431

Hernández-Origel, CD, Patiño-Saldivar, L, Salazar-Hernández, M, Ardila, AN, Talavera-López, A, Hernánez-Soto, R & Hernández, JA 2022, 'Use of Eichhornia crassipes as a bioadsorbent for the removal of methyl orange and methylene blue present in residual solutions', *Journal of Ecological Engineering*, vol. 23, pp. 193-211, https://doi.org/10.12911/22998993/151916

Ibrahim, M, Labaki, M, Giraudon, JM & Lamonier, JF 2020, 'Hydroxyapatite, a multifunctional material for air, water, and soil pollution control: A review', *Journal of Hazardous Materials*, vol. 383, article 121139, https://doi.org/10.1016/j.jhazmat.2019.121139

Javed, R, Zia, M, Naz, S, Aisida, SO, Ain, N ul & Ao, Q 2020, 'Role of capping agents in the application of nanoparticles in biomedicine and environmental remediation: Recent trends and future prospects', *Journal of Nanobiotechnology*, vol. 18, 172, pp. 1-15, https://doi.org/10.1186/s12951-020-00704-4

Kahrizi, P, Mohseni-Shahri, FS & Moeinpour, F 2018, 'Adsorptive removal of cadmium from aqueous solutions using NiFe2O4/hydroxyapatite/graphene quantum dots as a novel nano-adsorbent', *Journal of Nanostructure in Chemistry*, vol. 8, pp. 441-452, https://doi.org/10.1007/s40097-018-0284-3

Karamah, EF, Anindita, L, Amelia, D, Kusrini, E & Bismo, S 2019, 'Tofu industrial wastewater treatment with ozonation and the adsorption method using natural zeolite', *International Journal of Technology*, vol. 10, no. 8, pp. 1498-1504, https://doi.org/10.14716/ijtech.v10i8.3471

Kartika, R, Ritonga, AH, Sulastri, L, Nurnila, S, Irawan, D & Simanjuntak, P 2023, 'Biosorption of hexavalent chromium Cr(VI) using microalgae Scenedesmus sp as environmental bioindicator', *International Journal of Technology*, vol. 14, no. 4, pp. 791-799, https://doi.org/10.14716/ijtech.v14i4.5188

Khezami, L, Taha, KK, Ouldm'Hamed, M & Lemine, OM 2017, '(x)ZnO(1−x)Fe2O3 nanocrystallines for the removal of cadmium(II) and nickel(II) from water: Kinetic and adsorption studies', *Journal of Water Supply: Research and Technology – AQUA*, vol. 66, pp. 381-391, https://doi.org/10.2166/aqua.2017.033

Kusdianto, K, Widiyastuti, W, Shimada, M, Nurtono, T, Machmudah, S & Winardi, S 2019, 'Photocatalytic activity of ZnO–Ag nanocomposites prepared by a one-step process using flame pyrolysis', *International Journal of Technology*, vol. 10, no. 3, pp. 571-581, https://doi.org/10.14716/ijtech.v10i3.2902

Labanni, A, Zulhadjri, Handayani, D, Ohya, Y & Arief, S 2019, 'The effect of monoethanolamine as stabilizing agent in Uncaria gambir Roxb. mediated synthesis of silver nanoparticles and its antibacterial activity', *Journal of Dispersion Science and Technology*, vol. 0, pp. 1–8, https://doi.org/10.1080/01932691.2019.1626249

Labanni, A, Zulhadjri, Handayani, D, Ohya, Y & Arief, S 2020, 'Size controlled synthesis of well-distributed nano-silver on hydroxyapatite using alkanolamine compounds', *Ceramic International*, vol. 46, pp. 5850–5855, https://doi.org/10.1016/j.ceramint.2019.11.035

Lei, T, Li, SJ, Jiang, F, Ren, ZX, Wang, LL, Yang, XJ, Tang, LH & Wang, SX 2019, 'Adsorption of cadmium ions from an aqueous solution on a highly stable dopamine-modified magnetic nano-adsorbent', *Nanoscale Research Letters*, vol. 14, pp. 1–17, https://doi.org/10.1186/s11671-019-3154-0

Liu, F, Zhou, K, Chen, Q, Wang, A & Chen, W 2018, 'Comparative study on the synthesis of magnetic ferrite adsorbent for the removal of Cd(II) from wastewater', *Adsorption Science & Technology*, vol. 36, pp. 1456–1469, https://doi.org/10.1177/0263617418779729

Madkhali, N, Prasad, C, Malkappa, K, Choi, HY, Govinda, V, Bahadur, I & Abumousa, RA 2023, 'Recent update on photocatalytic degradation of pollutants in wastewater using TiO_2-based heterostructured materials', *Results in Engineering*, vol. 17, article 100920, https://doi.org/10.1016/j.rineng.2023.100920

Mohamed, WS, Alzaid, M, Abdelbaky, MSM, Amghouz, Z, García-Granda, S & Abu-Dief, AM 2019, 'Impact of Co^{2+} substitution on microstructure and magnetic properties of $Co_xZn_{1-x}Fe_2O^4$ nanoparticles', *Nanomaterials*, vol. 9, pp. 1-17, https://doi.org/10.3390/nano9111602

Mohammed, NAH, Shamma, RN, Elagroudy, S & Adewuyi, A 2024, 'Chitosan incorporated nickel ferrite photocatalyst for complete photocatalytic degradation of ciprofloxacin, ampicillin and erythromycin in water', *Results in Chemistry*, vol. 7, article 101307, https://doi.org/10.1016/j.rechem.2024.101307

Nayak, A & Bhushan, B 2021, 'Hydroxyapatite as an advanced adsorbent for removal of heavy metal ions from water: Focus on its applications and limitations', *Materials Today: Proceedings*, vol. 46, pp. 11029-11034, https://doi.org/10.1016/j.matpr.2021.02.149

Padhan, AM, Nayak, S, Sahu, M, Jagličić, Z, Koželj, P & Kim, HJ 2023, 'Cationic redistribution induced magnetic properties of Zn^{2+} substituted $MgFe_2O_4$ spinel ferrite', *Physica B: Condensed Matter*, vol. 668, article 415245, https://doi.org/10.1016/j.physb.2023.415245

Panda, S, Biswas, CK & Paul, S 2021, 'A comprehensive review on the preparation and application of calcium hydroxyapatite: A special focus on atomic doping methods for bone tissue engineering', *Ceramics International*, vol. 47, pp. 28122–28144, https://doi.org/10.1016/j.ceramint.2021.07.100

Paydar, S, Akbar, N, Shi, Q & Wu, Y 2020, 'Developing cuprospinel CuFe2O4–ZnO semiconductor heterostructure as a proton conducting electrolyte for advanced fuel cells', *International Journal of Hydrogen Energy*, vol. 46, no. 15, pp. 9927-9937, https://doi.org/10.1016/j.ijhydene.2020.04.198

Rafiq, A, Ikram, M, Ali, S, Niaz, F, Khan, M, Khan, Q & Maqbool, M 2021, 'Photocatalytic degradation of dyes using semiconductor photocatalysts to clean industrial water pollution', *Journal of Industrial and Engineering Chemistry*, vol. 97, pp. 111-128, https://doi.org/10.1016/j.jiec.2021.02.017

Rahmayeni, Azizah, N, Stiadi, Y, Putri, YE & Zulhadjri 2022, 'Magnetic particles nanorod of $ZnO/CuFe_2O_4$ prepared by green synthesized approach: Structural, optical and magnetic properties, and photocatalytic activity', *Materials Research*, vol. 25, pp. 1-11, https://doi.org/10.1590/1980-5373-MR-2021-0164

Rahmayeni, Febrialita, R, Stiadi, Y, Putri, YE, Sofyan, N & Zulhadjri 2021, 'Simbang Darah (*Iresine herbstii*) extract mediated hydrothermal method in the synthesis of zinc ferrite spinel nanoparticles used for photocatalysis and antibacterial applications', *Journal of Environmental Chemical Engineering*, vol. 9, no. 2, article 105140, https://doi.org/10.1016/j.jece.2021.105140

Rahmayeni, Putri, J, Stiadi, Y & Zulhadjri 2019, 'Green synthesis of $NiFe_2O_4$ spinel ferrites magnetic in the presence of Hibiscus rosa-sinensis leaves extract: Morphology, structure and activity', *Rasayan Journal of Chemistry*, vol. 12, pp. 1942–1949, https://doi.org/10.31788/RJC.2019.1245304

Rahmayeni, Wendari, TP, Ramadani, S, Stiadi, Y, Sofyan, N & Zulhadjri 2023, '$CuFe_2O_4$/hydroxyapatite magnetic nanocomposite synthesized using Pensi clam shells as a source of calcium for degradation of dye and anti-bacterial applications', *Case Studies in Chemical and Environmental Engineering*, vol. 8, pp. 1–10, https://doi.org/10.1016/j.cscee.2023.100482

Rimus, A, Hartati, W, Herry, A, Fathoni, A & Wendari, P 2024, 'Transforming seafood waste: Green mussel shell-derived hydroxyapatite as a catalyst for spirooxindole synthesis', *Bioresource Technology Reports*, vol. 25, article 101796, https://doi.org/10.1016/j.biteb.2024.101796

Sery, AA, El-Boraey, HA, Abo-Elenein, SA & ElKorashey, RM 2021, '$CuFe_2O_4$@hydroxyapatite composite for the environmental remediation of some heavy metal ions: Synthesis and characterization', *Water Science*, vol. 35, pp. 154-164, https://doi.org/10.1080/23570008.2021.1994242

Supriyono, Kartikowati, CW, Poerwadi, B, Wulandari, C, Hikma, LLF, Azzahra, A, Ghanyysyafira, K & Pinastika, HL 2023, 'The formation process of hydroxyapatite nanoparticles by electrolysis and their physical characteristics', *International Journal of Technology*, vol. 14, no. 2, pp. 330-338, https://doi.org/10.14716/ijtech.v14i2.4452

Suryawanshi, SM, Chandekar, KV, Badwaik, DS, Warhate, VV, Gahane, NM & Daf, SR 2023, 'Structural, surface, magnetic, and dielectric properties of $Ni_{0.3}Cu_{0.3}Zn_{0.4}Fe_{1.4}Cr_{0.6}O_4$ spinel ferrite nanocrystals prepared by sol-gel auto combustion route', *Inorganic Chemistry Communications*, vol. 156, article 111204, https://doi.org/10.1016/j.inoche.2023.111204

Tamjidi, S, Esmaeili, H & Kamyab Moghadas, B 2019, 'Application of magnetic adsorbents for removal of heavy metals from wastewater: A review study', *Materials Research Express*, vol. 6, no. 10, pp. 1-16, https://doi.org/10.1088/2053-1591/ab3ffb

Ubando, AT, Africa, ADM, Maniquiz-Redillas, MC, Culaba, AB, Chen, WH & Chang, JS 2021, 'Microalgal biosorption of heavy metals: A comprehensive bibliometric review', *Journal of Hazardous Materials*, vol. 402, article 123431, https://doi.org/10.1016/j.jhazmat.2020.123431

Ullah, R, Khitab, F, Gul, H, Khattak, R, Ihsan, J, Khan, M, Khan, A, Vincevica-Gaile, Z & Aouissi, HA 2023, 'Superparamagnetic zinc ferrite nanoparticles as visible-light active photocatalyst for efficient degradation of selected textile dye in water', *Catalysts*, vol. 13, article 1061, https://doi.org/10.3390/catal13071061

Wahyuni, S, Syukri, S & Arief, S 2019, 'Green synthesis of Ag/TiO2 nanocomposite assisted by gambier leaf (Uncaria gambir Roxb) extract', *Jurnal Kimia Sains dan Aplikasi*, vol. 22, pp. 250-255, https://doi.org/10.14710/jksa.22.6.250-255

Wang, ER & Shih, KY 2021, 'Facile microwave hydrothermal synthesis of ZnFe2O4/rGO nanocomposites and their ultra-fast adsorption of methylene blue dye', *Materials*, vol. 14, pp. 1-22, https://doi.org/10.3390/ma14185394

Wang, M, Zhang, K, Wu, M, Wu, Q, Liu, J, Yang, J & Zhang, J 2019, 'Unexpectedly high adsorption capacity of esterified hydroxyapatite for heavy metal removal', *Langmuir*, vol. 35, pp. 16111–16119, https://doi.org/10.1021/acs.langmuir.9b02373

Yadav, RS, Kuřitka, I, Vilcakova, J, Urbánek, P, Machovsky, M, Masař, M & Holek, M 2017, 'Structural, magnetic, optical, dielectric, electrical and modulus spectroscopic characteristics of $ZnFe_2O_4$ spinel ferrite nanoparticles synthesized via honey-mediated sol-gel combustion method', *Journal of Physics and Chemistry of Solids*, vol. 110, pp. 87-99, https://doi.org/10.1016/j.jpcs.2017.05.029

Yue, X, Huang, J, Jiang, F, Lin, H & Chen, Y 2019, 'Synthesis and characterization of cellulose-based adsorbent for removal of anionic and cationic dyes', *Journal of Engineered Fibers and Fabrics*, vol. 14, pp. 1-10, https://doi.org/10.1177/1558925019828194